Energy materials

CrossMark

Direct growth of Cu$_2$ZnSnS$_4$ on three-dimensional porous reduced graphene oxide thin films as counter electrode with high conductivity and excellent catalytic activity for dye-sensitized solar cells

Zhoujun Pang[1], Aixiang Wei[1,2], Yu Zhao[1,*], Jun Liu[1], Lili Tao[1], Ye Xiao[1], Yibing Yang[1], and Dongxiang Luo[1]

[1] *School of Material and Energy, Guangdong University of Technology, Guangzhou 510006, China*
[2] *Xinhua College, Sun Yat-Sen University, Guangzhou 510275, China*

ABSTRACT

Well-crystallized Cu$_2$ZnSnS$_4$ (CZTS) nanoparticles contain ultrasmall nanocrystals ($\sim$ 10 nm) have been grown directly on three-dimensional (3D) transparent porous reduced graphene oxide (rGO) thin films by a facile and scalable solution-based strategy. Few-layer rGO prepared by modified Hummers' method was used to fabricate hierarchical ultraporous 3D rGO thin films (3DGTFs) with high transmittance ($> 75\%$ for 200-nm thick). Single-phase kesterite CZTS nanocrystalline particles were grown uniformly on the surface active sites within the 3D rGO network by hydrothermal method. The as-prepared CZTS/rGO composite thin films exhibited excellent electrocatalytic ability by taking advantages of the high conductivity and high surface area of 3DGTFs and the high catalytic activity of CZTS nanoparticles. As expected, the composite thin films demonstrate more than one order of magnitude lower in electrical resistivity and in charge transfer resistance than the individual CZTS thin films. The conversion efficiency of dye-sensitized solar cells using CZTS/rGO thin films as the counter electrode (CE) approached 6.12%, comparable to that using Pt CE (6.45%) and superior to those using individual CZTS CE (1.07%) and rGO CE (0.18%).

Introduction

Dye-sensitized solar cells (DSSCs) have recently received great attention due to their reasonable high power conversion efficiency, ease of fabrication, and cost-effectiveness [1–3]. A typical DSSC consists of a photosensitized anode, an electrolyte, and a counter electrode (CE). The counter electrode is an important component in DSSCs, because it collects the electrons from the external circuit and allows the I_3^- reduction reaction. Pt is the most widely used CE in DSSCs due

Address correspondence to E-mail: zhaoyu@gdut.edu.cn

to its high electrocatalytic activity and good electrical conductivity. However, its limited reserves and high cost restrict the scalability of DSSCs. Thus, researchers are dedicated to look for alternative low-cost CE materials possessing conductivity and electrocatalytic activity similar to that of Pt. Recently, CZTS has also been explored as catalytic materials for CE in DSSCs [4–8]. The conversion efficiency of DSSCs with CZTS CE is reported to be close [5, 8] or even superior [4, 6, 7] to that with Pt CE. Even CZTS has excellent catalytic activity, its low electrical conductivity, commonly three orders of magnitude lower than that of Pt, is still the limitation for the improvement of its electrocatalytic activity. Therefore, enhancing the conductivity of CZTS thin film as CE is crucial to the high performance of DSSCs. To overcome this obstacle, several works have focused on the incorporation of CZTS into highly conductive nanostructured carbons [9–11]. Graphene represents an excellent backbone to accommodate such quaternary chalcogenide, because of its outstanding features of high conductivity and high specific surface area. Due to the increase of active material per projected area, three-dimensional (3D) graphene exhibits additional characteristics such as high mechanical strength, superior high surface area, multidimensional electron transport pathways, easy access to the electrolyte, and minimized transport distances between the bulk electrode and the electrolyte [12, 13]. Furthermore, the graphene sheets in 3D framework are highly interconnected and interlocked together to prevent them from restacking. Therefore, 3D graphene has become one of the most appealing matrices for catalytic materials. Nevertheless, all the CZTS/graphene composite reported so far is in the form of powders prepared by either the simple mixing of CZTS and graphene (or rGO) [9, 10] or in-suit growing of CZTS onto rGO powders [11]. Even those reported procedure to prepare CZTS/graphene or CZTS/rGO composite was simple when the mixing powders were spin-coated in thin films for device fabrication, it results in relatively inadequate conductivity because the electrical transport pathway is not constructed by conductive rGO but CZTS/rGO composite. A direct coating of graphene or rGO thin films on the conductive substrate is preferable as it provides superior electrical contact to the substrate and simplifies the process of device fabrication. Also, the direct growth or decoration of catalytic materials on the surface or in the interspace of substrate-supported 3D graphene or rGO network will be desired to obtain high conductivity and high catalytic activity simultaneously. However, it remains a challenge to this day.

In this work, distinguished from previous methods of preparing CZTS/rGO composite, we designed a facile and scalable solution-based strategy to grow CZTS nanoparticles on 3D porous rGO thin films directly. First, few-layer rGO prepared by modified Hummers' method was coated in the transparent conductive fluorine-doped tin oxide (FTO) substrates by the screen printing technique and post-heat treatment to form a 3DGTFs. Second, a simple hydrothermal method is used to synthesize single-phase and uniform-distributed CZTS nanoparticles within the aperture of 3D rGO network. Finally, CZTS/graphene thin films were used as advanced CE for DSSCs to achieve an improved device performance. Our strategy to prepare graphene-based composite thin films is all solution-based, very effective in reducing the cost for cell production. Additionally, it could be easily induced to the formation of other catalytic materials grown on conductive carbon matrices. Moreover, in the 3D composite framework, the high conductivity, high surface area, and porous structure ensure high utilization of active materials and the required conductivity as counter electrode, which is beneficial for the performance of DSSCs.

Experimental details

Synthesis of the 3DGTFs and CZTS/rGO composite thin films

Reduced graphene oxide (rGO) powder was obtained by the reduction of oxidized graphene powder according to the modified Hummers' method (see the synthesis in the ESI). The rGO powder was used as start material to make rGO paste by the following steps. First, 0.9 g ethyl cellulose was mixed with 8.0 g ethanol; then, a mixture solution of 9.6 g terpineol in 8.1 g ethanol was added drop by drop. After that, 100 mg rGO powder was added and then dispersed by stirring and sonication. Ethanol was then removed by evaporator at 50 °C. Finally, the rGO paste can be obtained when 0.6 ml diacetylmethane and 0.6 ml emulsifier OP were mixed and stirred with a 4-cm-long magnet tip at 300 rpm.
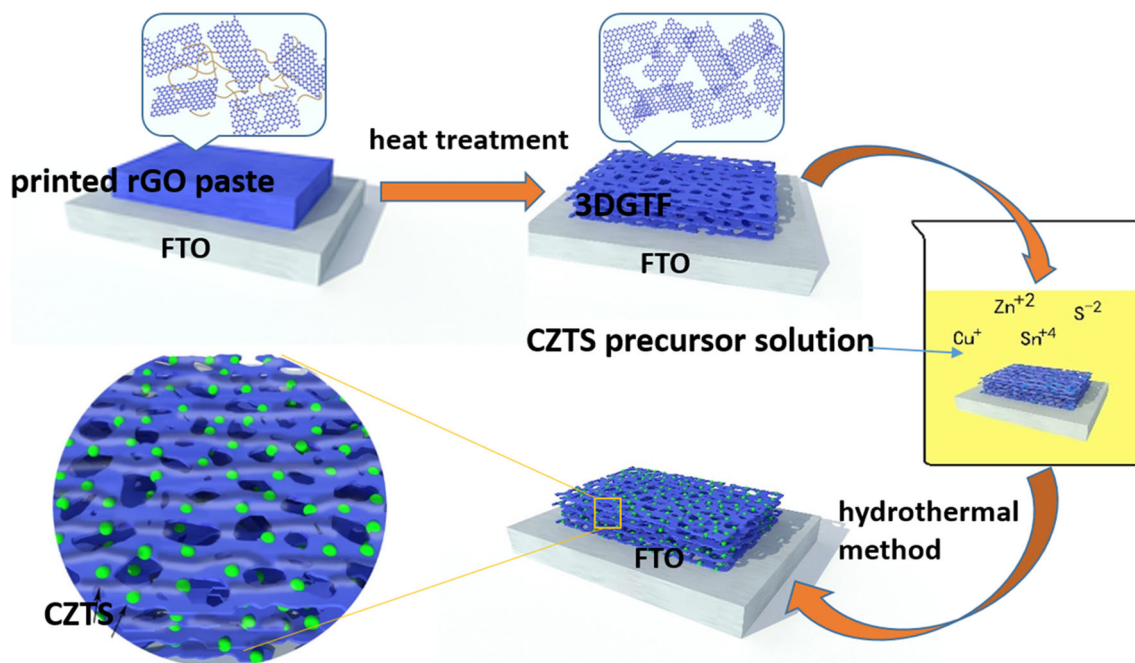
Scheme 1 Schematic illustration of the preparation process for the CZTS/rGO composite thin films on FTO glass.

The 3DGTFs prepared through a simple two-step synthesis process (Scheme 1). First, the rGO paste was coated on the FTO glass plates by screen printing, and then, a following drying was conducted for 10 min at 100 °C. This above procedure (with coating and drying) was repeated several times to increase the thickness of the 3DGTFs. We repeat the printing for four times in our study to obtain a thickness of about 200 nm. Second, the 3DGTFs was achieved after a heating in blast drying oven at 350 °C in air for 30 min.

CZTS/rGO composite thin films were fabricated by a simple hydrothermal method, which is shown in Scheme 1. The typical synthesis process is as follows: 1 mmol of copper (II) chloride dihydrate ($CuCl_2 \cdot 2H_2O$), 2 mmol of zinc(II) chloride ($ZnCl_2$), 0.5 mmol of tin (II) chloride dihydrate ($SnCl_2 \cdot 2H_2O$), 10 mmol of thiourea (CH_4N_2S), 2.8 mmol of oxalic acid ($H_2C_2O_4$), and 0.25 mmol of hexadecyl trimethyl ammonium bromide (CTAB) were dissolved, mixed, and stirred in 40 ml of ethanol as the precursor solution. The 3DGTFs on FTO glass was placed in a 60 ml Teflon liner, and the precursor solution was added to immerse the FTO glass. The hydrothermal process was subsequently performed at 200 °C for 12 h. After that, the autoclave was cooled down to room temperature. The FTO substrate was taken out, rinsed extensively with deionized water,

and dried in ambient air. The CZTS counter electrode was fabricated using the similar method.

DSSC assembling

A DSSC was fabricated with a dye-sensitized TiO_2 photoanode; a CE and a redox electrolyte injected into the gap between the photoanode and CE. (Detailed procedures of TiO_2 photoanode fabrication can be seen in ESI.) The dye-sensitized TiO_2 photoanode and counter electrode were assembled into a sandwich cell and sealed with a 60 μm in thick hot-melt gasket made of ionomer Surlyn 1170-60 (SOLARONIX SA). A square aperture of 6 mm × 6 mm with a diagonal passageway of 1 mm in width was cut out. A drop of the electrolyte (DHS-Et23) was injected into the cell via the reserved passageway.

Characterization and measurements

The sample of independent rGO for atomic force microscopy (AFM, Bruker Dimension Edge system) observations was prepared by spin-coating dilute suspensions of rGO on polished silicon wafer. Scanning electron microscopy (SEM) images were collected on a field emission scanning electron microscope (SU8010, Hitachi). X-ray diffraction

(XRD) measurements were carried out on a D/MAX-UltimaIV (Rigaku Co., Japan) using Cu-Ka radiation (λ = 0.1542 nm) with a scan rate of $10°\text{min}^{-1}$ at 40 kV and 30 mA. Transmission electron microscopy (TEM) investigations carried out on a JEOL JEM-2100 (HR) at 200 kV. Raman spectroscopy was performed on a LabRAM HR 800 UV Laser micro-Raman Spectroscopy (HORIBA Jobin–Yvon, France). Fourier transform infrared spectroscopy (FTIR) was obtained by using a Nicolet 6700 Fourier Transform Infrared Spectroscopy (Nicolet, USA). The photovoltaic measurements were performed using an AM1.5 solar simulator (500 W xenon lamp, NBeT, Solar-500) with an intensity of 100 mW/cm². The photocurrent–voltage (J–V) curves were recorded using a Keithley model 2400 source measurement unit. Electrochemical impedance spectroscopy (EIS) and Tafel polarization were performed with a symmetrical cell, which consists of two same CEs, using an electrochemical workstation (ZAHNER-IM6). The EIS was carried out under the 0 V DC bias voltages and frequency ranged from 50 mHz to 1000 kHz, while the AC magnitude was set at 10 mV. The transmittance of rGO thin films was performed using an ultraviolet spectrophotometer (T6, Beijing Purinje General Instrument).

Results and discussion

AFM micrographs of rGO flake suggest that the thinnest rGO flake and its wrinkle consist of single-layer rGO, detail of which can be seen in ESI. As shown in the SEM images of Fig. 1c, e, and g, the 3DGTFs prepared from such single-layer or few-layer rGO powder possesses ultraporous and hierarchical structure, as a result of the volatilization of the mixed organic solvent at high temperature. Such morphology endows large surface area and large volume of interspace for the further growth of catalytic materials. The 3DGTFs also shows an excellent transparency. For example, transmittance of 76% was found at 550 nm for 200-nm-thick 3DGTFs, indicating the very large volume of interspace and ultraporous structure of the 3DGTFs (ESI reveals more details). CZTS nanoparticles were in situ grown on the surface and in the interspace of the 200-nm-thick 3DGTFs by hydrothermal method. The macroscopical photograph of the samples was shown in Fig. 1b, and the front and cross-sectional microscopic images of CZTS/rGO composite were shown in

Fig. 1d, f, h. The thickness of the composite thin films did not vary obviously after the growth of CZTS nanoparticles because most of the product was grown on surface defective sites and edges within 3D rGO network. Inherited from the 3DGTFs, the composite films also possess large surface area and porous structure. Such structure is very suitable for the use of CE, as it could have significant benefit for electrolyte penetration within the electrode networks, giving the electrolyte more access to CZTS surface. The well-distributed CZTS nanoparticles were in diameter about 250 nm on average and composed of many small nanocrystals.

Fourier transform infrared spectroscopy (FTIR) was used to indicate the variation of chemical structure in 3DGTFs during the fabrication process. For comparison, the 3DGTFs and the organic paste with and without the mixing of rGO powder were investigated. As indicated in Fig. 2, the FTIR spectrum for pure paste without rGO showed a representative spectrum of ethyl cellulose with characteristic peaks for –CH stretching at 2873 and 2975 cm⁻¹ and –OH stretching peak at 3485 cm⁻¹. The other important peaks at 1104 and 1375 cm⁻¹ were mainly corresponded to C–O–C stretch and C–H bending, respectively [14]. The 880 and 920 cm⁻¹ peak was assigned to ethyl group characteristic absorption. The peak around 880 and 920 cm⁻¹ was almost vanished in paste sample with rGO, indicating interactions between rGO and ethyl cellulose. The possible mechanism is that the dangling bonds of defective rGO replace the ethyl group in cellulose chain, resulting in a cross-linked paste, as schematically shown in Scheme 1. The FTIR spectrum of 3DGTFs showed only two clearly visible peaks at 1618 and 3420 cm⁻¹, indicating the removal of organic matter in the paste after heat treatment. The peak at 1618 cm⁻¹ is assigned to skeletal vibrations of the unoxidized graphitic domains [15], while the peak at 3420 cm⁻¹ could be due to the O–H stretching mode of intercalated water. The intensity of peak at 1618 cm⁻¹ was sharper in comparison with that of paste sample with rGO, implying an enhanced strength of C–C bonding. The above results indicate that heat treatment is a critical process to remove the organic component and enhance the cross-link of rGO flakes.

The high magnification SEM image, TEM image, HRTEM image, and SAED of composite thin films were shown in Fig. 3, further confirming that CZTS
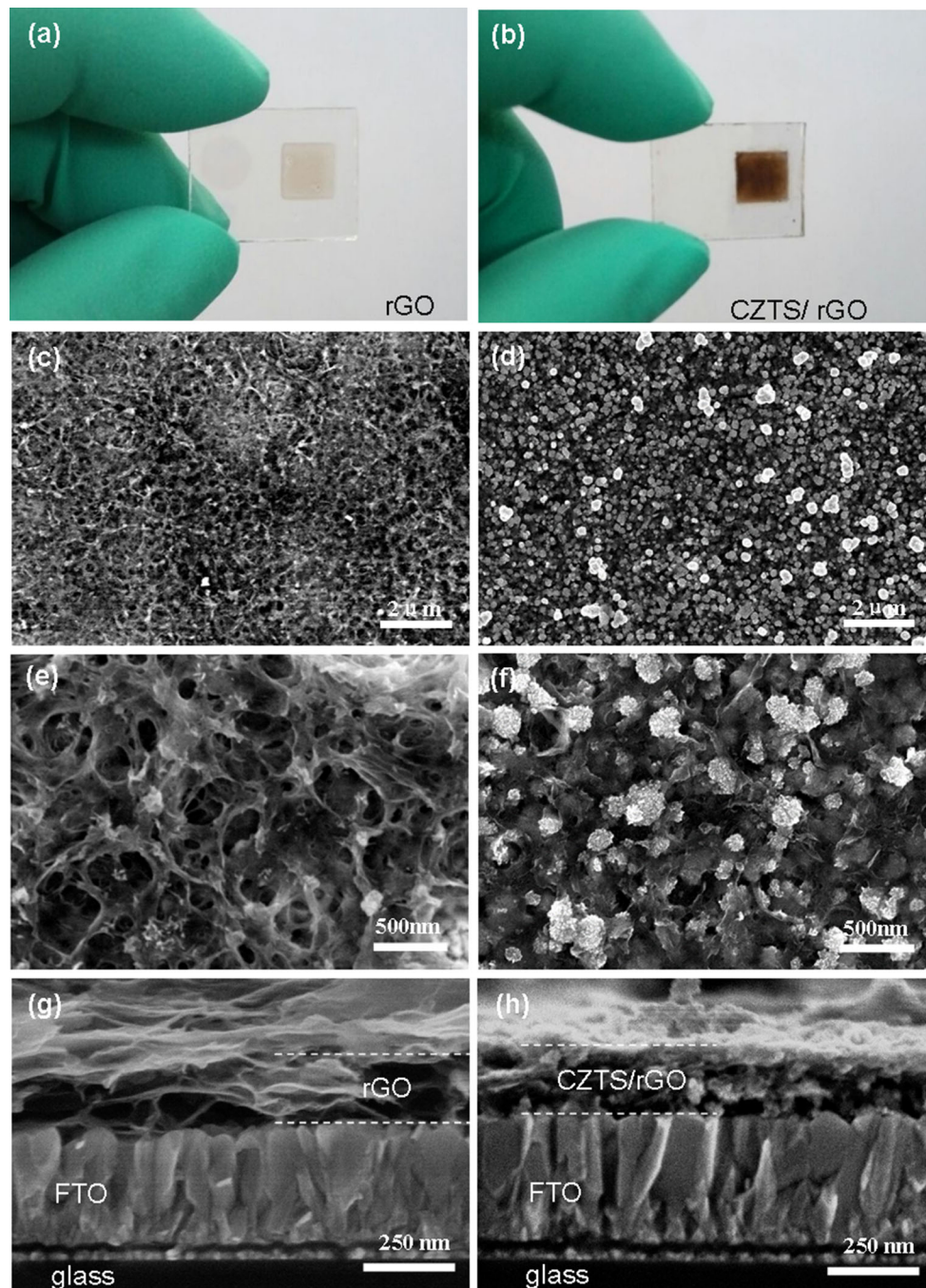
Figure 1 Photograph of **a** 3DGTFs and **b** CZTS/rGO thin films on FTO glass. Plane view SEM image of **c**, **e** 3DGTFs and **d**, **f** CZTS/rGO thin films. Cross-sectional SEM image of **g** 3DGTFs and **h** CZTS/rGO thin films on FTO glass. 3DGTFs is labeled as rGO in the figure.

nanoparticles were in situ grown on the surface of rGO flake. Figure 3a shows CZTS nanoparticles grown on surface defective sites and edges within 3D rGO network. As revealed in Fig. 3b, the CZTS nanoparticles grown on rGO flake were composed of a large number of nanocrystals with average size about 10 nm (see Fig. S2 (b) in ESI for more details). The concave–convex surface and discontinuous lattice indicate that the spherical particle is aggregate of small size nanocrystals (see where the white arrow pointed). Hence, the as-synthesized CZTS nanoparticles can be referred to as nanocrystalline [16]. The
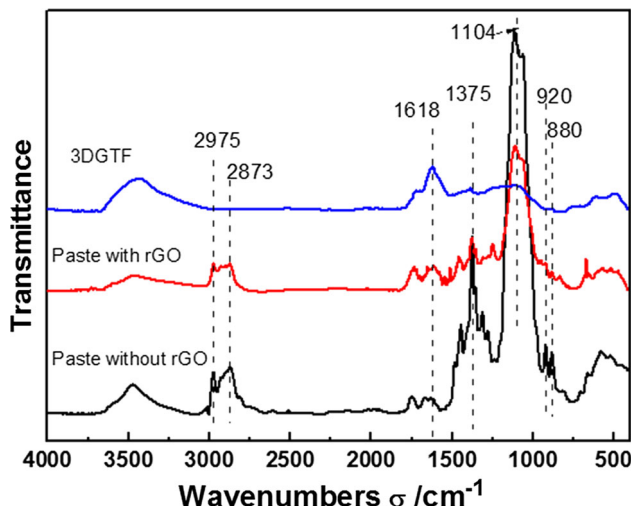
Figure 2 FTIR spectrum of three samples, the 3DGTFs, the paste with and without rGO powder.

magnified HRTEM image of the nanocrystals in Fig. 3c revealed its well-defined lattice fringes and detailed crystallographic structure. The lattice spacing of 0.31 nm corresponds to the (112) plane of the kesterite structure CZTS. The bright diffraction spots shown in the inset of Fig. 3c indicate the good crystalline quality of CZTS nanocrystalline. Moreover, the CZTS nanoparticles and rGO were also confirmed by elemental SEM mapping, as shown in Fig. 3d1–d6. The element of Cu, Zn, Sn, S, and C exists in the composite thin films, corresponding to the element of CZTS and rGO. However, the great amount of Sn and O derived from the FTO glass makes it difficult to determine the molar ratio of Sn in CZTS. Nevertheless, result from the EDS spectrum (Fig. S3 in ESI) exhibits molar ratio of [Cu]: [Zn]: [S] = 2.46: 1: 3.53, close to the stoichiometric molar ratio of Cu_2ZnSnS_4.
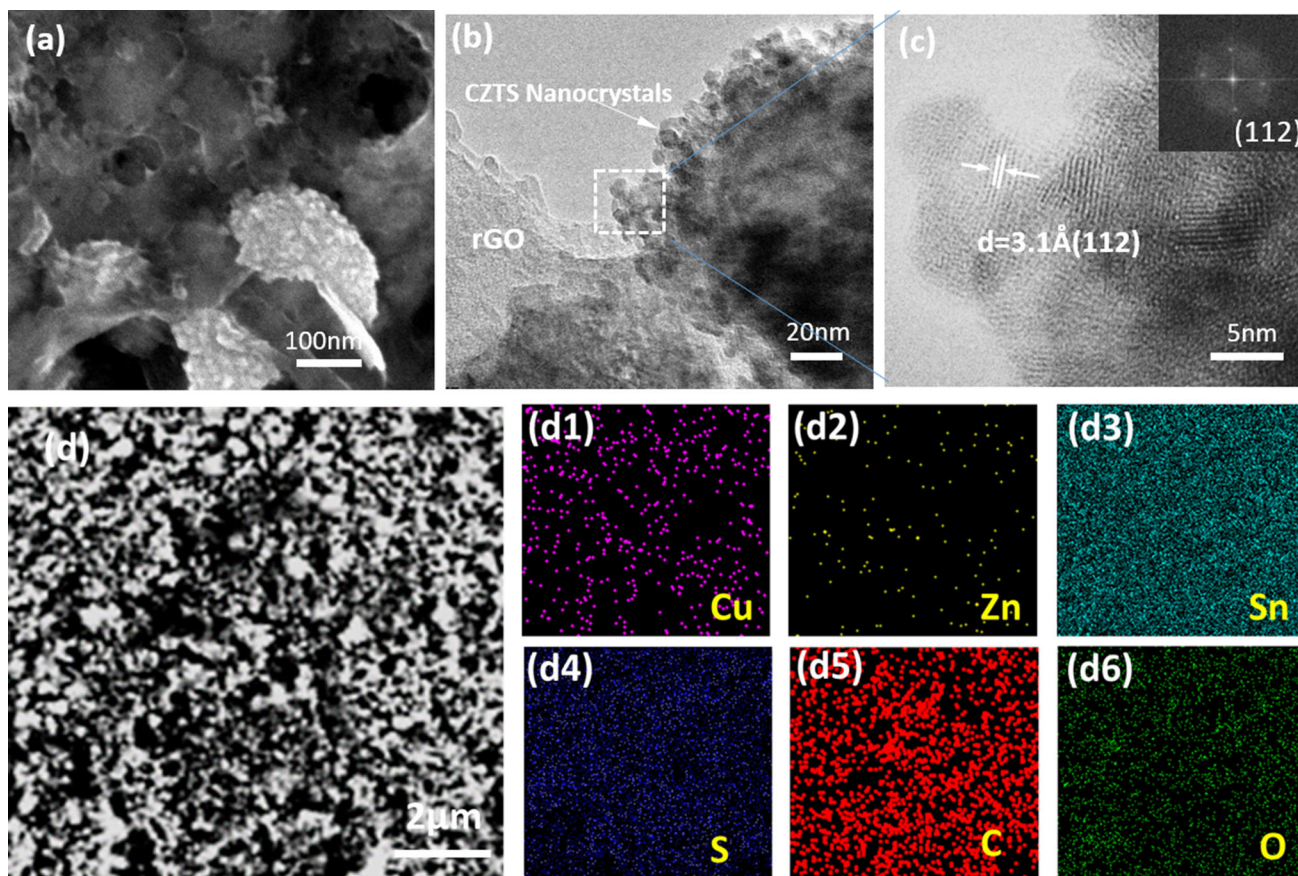

Figure 3 Microscopic characterizations of the CZTS/rGO thin films: **a** high magnification SEM image, **b** TEM image, **c** HRTEM image. The inset is the SAED pattern of the nanoflakes shown in **c**, **d** SEM image, and energy dispersive X-ray spectroscopy (EDS) elemental maps for copper (**d1**), zinc (**d2**), tin (**d3**), sulfur (**d4**), carbon (**d5**), and oxygen (**d6**).

Figure 4 a XRD and
b Raman spectra of CZTS/
rGO thin films, CZTS thin
films, and rGO thin films on
FTO glass.
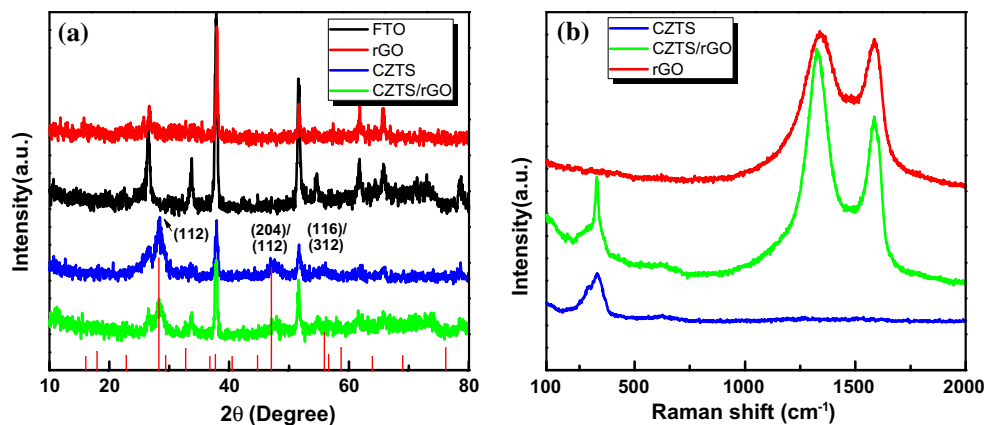
To further confirm the structure and the composition of the composite, XRD and Raman spectroscopy were used to characterize the composite thin films on FTO glass. The XRD pattern of 3DGTFs (labeled as rGO in the figure) in Fig. 4a shows no remarkable peak except the characteristic diffraction peak of FTO. This is another evidence that the 3DGTFs consists of few-layer rGO because the disappearance of diffraction peak represents the disordered stacking of graphene thinned to several layers [16, 17]. In the XRD spectrum of individual CZTS and CZTS/rGO samples, the major diffraction peaks appeared at around $2\theta = 28.4°$, 47.2° and 56.1° can be indexed (112), (220) and (312) of the kesterite crystal structure of CZTS (JCPDS no. 26-0575). No obvious peaks resulting from impurities were observed except for those peaks from FTO substrate. The average crystallite sizes of the CZTS nanocrystalline calculated using well-known Debye–Scherer equation (see the ESI for details) based on the (112) peaks are approximately 8 nm, slightly smaller than the observation from HRTEM image, indicating again the very small size of the CZTS nanocrystals.

Raman spectroscopy was used to further confirm the phase of the composite samples, especially when XRD is insufficient to identify most of the minor phases of CZTS. Figure 4b shows the Raman spectra of various thin films. The existence of rGO is confirmed by the presence of a G band ($\sim$ 1584 cm^{-1}) and a D band ($\sim$ 1334 cm^{-1}) for individual rGO films. The G band arises primarily from the E_{2g} vibration mode of sp^2 carbon, and the D band originates from the defects and disordered structure of sp^2 carbon [18]. The D band to G band ratios, viz., I_D/I_G, for rGO and CZTS/rGO are 1.13 and 1.38, respectively. The high I_D/I_G of CZTS/rGO implies the increased disorder of rGO induced by

the in situ growth of CZTS on its defect sites under the hydrothermal condition [19, 20]. The slight right shifts of the G band ($\sim$ 1586 cm^{-1}) of CZTS/rGO are likely due to the doping effects of CZTS [21, 22]. The existence of CZTS is confirmed by the intense peak at 333 cm^{-1} for individual CZTS thin films and 330 cm^{-1} for CZTS/rGO films, which are characteristic Raman peaks of the kesterite structure CZTS in bulk [8, 17] and in particles [7, 9], respectively. Such a Raman peak shift of CZTS nanoparticles is due to a decrease in phonon frequency for the A1 vibrational mode associated with particle size [23], phenomenon of which is found in many of the other reports of CZTS particle [24–26]. The characteristic Raman peaks of 330–333 cm^{-1} arise from A1 vibration mode of lattice, where the group VI atoms (S) vibrate while the rest of atoms remain fixed. Other compounds and mixed-phase impurity peaks, such as Cu$_3$SnS$_4$ (318, 348 and 295 cm^{-1}), Cu$_{2-x}$S (475 cm^{-1}), and ZnS (351 and 274 cm^{-1}), were not observed in the CZTS Raman spectra, suggesting that the nanoparticles grown on the 3DGTFs were purely CZTS phases.

To further elucidate the electrochemical behavior of CE-based interfaces, EIS analysis and Tafel polarization curve measurement of symmetrical dummy cells based on Pt, CZTS/rGO, CZTS, and rGO electrodes were measured and compared. Figure 5a shows the equivalent circuit and EIS Nyquist plots obtained by the symmetrical dummy cells, in which a thin layer of electrolyte solution is sandwiched between two identical electrodes. R_{ct} is related to the left semicircle on high-frequency region and mainly can be affected by two key parameters: One is the surface area, and the other is electrocatalytic activity of CE for the reduction of I^-/I^{3-}. R_s is easily obtained from the intercept of the horizontal axis at high-frequency end, and it is influenced by external wire

Figure 5 a Nyquist plots and **b** Tafel polarization curves of the symmetrical cells fabricated with CZTS/rGO CE, CZTS CE, rGO CE, and Pt CE. Inset in the Nyquist plots is the electrical equivalent circuit model used for data fitting.
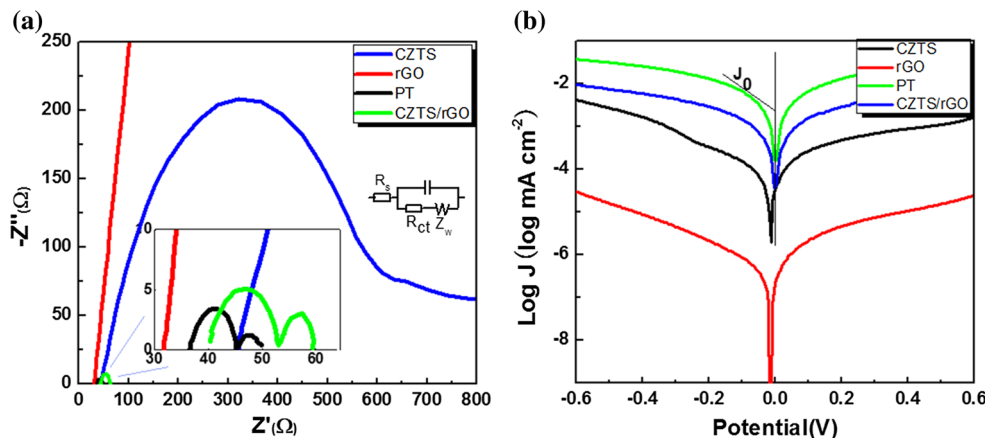

Table 1 Electrochemical parameters, electrical resistivity, average roughness, and the photovoltaic parameters of DSSCs assembled by using different CE

CE	ρ (Ω m)	R_s (Ω)	R_{ct} (Ω)	R_a (nm)	J_{SC} (mA/cm^2)	V_{oc} (V)	FF	PCE (%)
Pt	10.62	37.12	8.626	9.20	14.77	0.75	0.58	6.45
rGO	10.09	36.19	1.03×10^5	31.2	2.58	0.79	0.09	0.18
CZTS	73879	51.35	546.2	50.5	4.54	0.66	0.36	1.07
CZTS/rGO	4739	44.65	17.31	56.4	14.82	0.72	0.57	6.12

resistance, FTO glass resistance, conductivity of CE, and so on. The surface morphology of various samples was also measured by AFM technique (see Fig. S4 in ESI for details). Table 1 sums up the value of R_{ct} and R_s extracted from Fig. 5a, as well as the average roughness R_a calculated from AFM image. CZTS/rGO shows the largest surface roughness of 65.4 nm, implying that the morphology of CZTS/rGO consisted of nanoparticles and porous network has superior contact surface area for the electrolyte and electrode. CZTS/rGO and Pt CE show much smaller R_{ct} values than CZTS and rGO, suggesting that CZTS/rGO possesses superior electrocatalytic ability compared with its individual counterpart. Especially, R_{ct} of CZTS/rGO is more than one order of magnitude lower than that of CZTS, implying that the 3DGTFs network provides an effective pathway for the charge transfer between the electrolyte and electrode. The large volume of interspace in 3DGTFs ensures large-area growth of CZTS nanocrystalline and thus provides substantial active sites. As shown in Table 1 and the enlarged image from the selected area of Fig. 5a, the values of R_s were in the order rGO < Pt < CZTS/rGO < CZTS, confirming an improvement in conductivity with 3DGTFs.

Figure 5b shows Tafel polarization curves of the symmetrical dummy cells based on Pt, CZTS/rGO, CZTS, and rGO electrodes. The exchange current density J_0 is the slope of the Tafel polarization zone, and it varies inversely with R_{ct} of the electrode as it can be described in terms of the following Eq. (1). As shown in Fig. 5b, the anodic and cathodic branches of CZTS/rGO exhibit an obvious larger slope than those of CZTS and rGO, confirming the superior electro-catalytic ability of CZTS/rGO thin films.

$$J_0 = \frac{RT}{nFR_{ct}} \tag{1}$$

where T is the absolute temperature, R is the gas constant, F is the Faraday constant, and n is the total number of electrons involved in the reaction.

Other than electrocatalytic ability, the sheet resistance of the CE is another critical factor that affects the current density and power conversion efficiency (PCE) of DSSCs. Therefore, we measured the electrical resistivity ρ for different thin films through the simple ohmic method (described in EIS) and listed the results in Table 1 for comparison. As superior metal material, Pt and rGO possess low resistivity of about 10 Ω m. However, as a semiconductor without intended doping, CZTS exhibits a very large resistivity of 7.4×10^4 Ω m. Benefited from the effective conducting pathway constructed by 3DGTFs, CZTS/rGO has a reduced resistivity of 4.7×10^3 Ω m, one order of magnitude lower than that of individual CZTS, thus is very promising as CE in enhancing the performance of DSSCs.
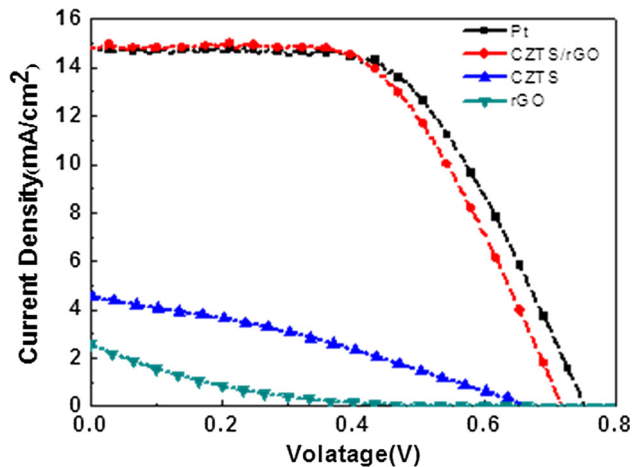
Fig. 6 J–V characteristics of the DSSCs assembled with CZTS/rGO CE, CZTS CE, rGO CE, and Pt CE.

As shown in Fig. 6, J–V characteristics of the DSSCs based on Pt, rGO, CZTS, and CZTS/rGO CEs were tested under illumination of $100 \, \text{mW/cm}^2$ (AM 1.5 G), and the detailed parameters of open-circuit voltage (V_{OC}), short-circuit current density (J_{SC}), fill factor (FF), and power conversion efficiency (PCE) are shown in Table 1. The CZTS/rGO CE-based DSSC has a good photovoltaic performance ($J_{SC} = 14.82 \, \text{mA/cm}^2$, $V_{OC} = 0.72$ V, FF $= 0.57$, PCE $= 6.12\%$), which is better than that of pure CZTS-based DSSC. Compared with Pt CE-based DSSC ($J_{SC} = 14.58 \, \text{mA/cm}^2$, $V_{OC} = 0.76$ V, FF $= 0.58$, PCE $= 6.45\%$), the CZTS/rGO-based CE has a slightly lower FF but higher J_{SC}, which results in a comparable PCE. The PCEs of pure CZTS-based cells decreased to much smaller value, which may be attributed to the higher overall resistances, and the PCEs of rGO-based cells are much inferior as a result of its lower catalytic activity for I^{3-} reduction though it shows a high V_{OC} of 0.79 V. The outstanding improvement of the efficiency clearly indicates the important role of the 3DGTFs. Its rich active sites and porous structure ensure multidimensional electron transport pathways, allowing high affinity to iodide mediator, high catalytic activity for I^{3-} reduction, and more abundant I^- for dye regeneration.

Conclusions

An all solution-based strategy, involving the preparation of few-layer rGO powder, fabrication of 3DGTFs, and in-suit growth of CZTS nanocrystalline

particles, was developed. The 3DGTFs fabricated from few-layer rGO flake and wrinkle exhibits 3D hierarchical ultraporous structure with thickness-dependent high transparency. Flower-like CZTS nanoparticles in singe kesterite phase consist of ultrasmall nanocrystals of approximately 10 nm in crystallite size were uniformly grown on active surface cite within the 3DGTFs. The as-prepared CZTS/rGO composite thin films exhibited excellent electrocatalytic ability with both electrical resistivity ρ and charge transfer resistance R_{ct} one order of magnitude lower than that of individual CZTS counterpart. By combining the advantages of the high conductivity and high surface area of the 3DGTFs and the high catalytic activity of CZTS nanoparticles, the DSSCs using CZTS/rGO thin films as the counter electrode demonstrate conversion efficiency of 6.12%, very close to that of 6.45% using Pt CE, and superior to that of 1.07 and 0.18% using individual CZTS CE and rGO CE, respectively. Our study provides a practical approach for the low-cost fabrication of high-quality graphene composite thin films and sheds light on its potential application in optoelectronic devices.

Compliance with ethical standards

Conflict of interest All the authors declare that they have no conflict of interest.

Electronic supplementary material:
The online version of this article (doi:10.1007/s10853-017-1741-y) contains supplementary material, which is available to authorized users.

References

[1] Hagfeldt A, Boschloo G, Sun LC, Kloo L, Pettersson H (2010) Dye-sensitized solar cells. Chem Rev 110:6595–6663

[2] Gratzel M (2005) Solar energy conversion by dye-sensitized photovoltaic cells. Inorg Chem 44:6841–6851

[3] Wu JH, Lan Z, Lin JM, Huang ML, Huang YF, Fan LQ, Luo GG (2015) Electrolytes in dye-sensitized solar cells. Chem Rev 115:2136–2173

[4] Xin XK, He M, Han W, Jung JH, Lin ZQ (2011) Low-cost copper zinc tin sulfide counter electrodes for high-efficiency dye-sensitized solar cells. Angew Chem Int Ed 50:11739–11742

[5] Fan MS, Chen JH, Li CT, Cheng KW, Ho KC (2015) Copper zinc tin sulfide as a catalytic material for counter electrodes in dye-sensitized solar cells. J Mater Chem A 3:562–569

[6] Mali SS, Patil PS, Hong CK (2014) Low-cost electrospun highly crystalline kesterite cu_2znsns_4 nanofiber counter electrodes for efficient dye-sensitized solar cells. ACS Appl Mater Interfaces 6:1688–1696

[7] Wozny S, Wang K, Zhou W (2013) Cu_2ZnSnS_4 nanoplate arrays synthesized by pulsed laser deposition with high catalytic activity as counter electrodes for dye-sensitized solar cell applications. J Mater Chem A 1:15517–15523

[8] Liu J, Luo FZ, Wei AX, Liu Z, Zhao Y (2015) In-situ growth of Cu_2ZnSnS_4 nanospheres thin film on transparent conducting glass and its application in dye-sensitized solar cells. Mater Lett 141:228–230

[9] Bai L, Ding JN, Yuan NY, Hu HW, Li Y, Fang X (2013) Cu_2ZnSnS_4/graphene composites as low-cost counter electrode materials for dye-sensitized solar cells. Mater Lett 112:219–222

[10] Tang QT, Shen HL, Yao HY, Wang W, Jiang Y, Zheng CF (2016) Synthesis of CZTS/RGO composite material as supercapacitor electrode. Ceram Int 42:10452–10458

[11] Thangaraju D, Karthikeyan R, Prakash N, Babuc SM, Hayakawa Y (2015) Growth and optical properties of Cu_2ZnSnS_4 decorated reduced graphene oxide nanocomposites. Dalton Trans 44:15031–15041

[12] Nardecchia S, Carriazo D, Ferrer ML, Gutierrez MC, del Monte F (2013) Three dimensional macroporous architectures and aerogels built of carbon nanotubes and/orgraphene: synthesis and applications. Chem Soc Rev 42:794–830

[13] Li YY, Zhang HY, Wang SX, Lin YX, Chen YM, Shi ZC, Li N, Wang WG, Guo ZP (2016) Facile low-temperature synthesis of hematite quantum dots anchored on a three-dimensional ultra-porous graphene-like framework as advanced anode materials for asymmetric supercapacitors. J Mater Chem A 4:11247–11255

[14] Suthar V, Pratap A, Raval H (2000) Studies on poly (hydroxy alkanoates)/(ethylcellulose) blends. Bull Mater Sci 23:215–219

[15] Shen XP, Wu JL, Bai S, Zhou H (2010) One-pot solvothermal syntheses and magnetic properties of graphene-based magnetic nanocomposites. J Alloys Compd 506:136–140

[16] McAllister MJ, Li JL, Adamson DH, Schniepp HC, Abdala AA, Liu J, Herrera-Alonso M, Milius DL, Car R, Prud'homme RK, Aksay IA (2007) Single sheet functionalized graphene by oxidation and thermal expansion of graphite. Chem Mater 19:4396–4404

[17] Eda G, Fanchini G, Chhowalla M (2008) Large-area ultra-thin films of reduced graphene oxide as a transparent and flexible electronic material. Nat Nanotechnol 3:270–274

[18] Pimenta MA, Dresselhaus G, Dresselhaus MS, Cancado LG, Jorio A, Saito R (2007) Studying disorder in graphite-based systems by Raman spectroscopy. Phys Chem Chem Phys 9:1276–1291

[19] Ferrari AC, Robertson J (2000) Studying disorder in graphite-based systems by Raman spectroscopy. Phys Rev B 61:14095–14107

[20] Dresselhaus MS, Eklund PC (2000) Phonons in carbon nanotubes. Adv Phys 49:705–814

[21] Dong XC, Fu DL, Fang WJ, Shi YM, Chen P, Li LJ (2009) Doping single-layer graphene with aromatic molecules. Small 5:1422–1426

[22] Dong XC, Wang JX, Wang J, Chan-Park MB, Li XG, Wang LH, Huang W, Chen P (2012) Supercapacitor electrode based on three-dimensional graphene-polyaniline hybrid. Mater Chem Phys 134:576–580

[23] Nien Y, Zaman B, Quyang J, Chen I, Hwang C, Yu K (2008) Raman scattering for the size of CdSe and CdS nanocrystals and comparison with other techniques. Mater Lett 62:4522–4524

[24] Kumar RS, Ryu BD, Chandramohan S, Seol JK, Lee SK, Hong CH (2012) Rapid synthesis of sphere-like Cu_2ZnSnS_4 microparticles by microwave irradiation. Mater Lett 86:174–177

[25] Wang W, Shen H, Yao H (2015) Influence of solution temperature on the properties of Cu_2ZnSnS_4 nanoparticles by ultrasound-assisted microwave irradiation. J Mater Sci Mater Electron 26:1449–1454

[26] Flynn B, Wang W, Chang C, Herman GS (2012) Microwave assisted synthesis of Cu_2ZnSnS_4 colloidal nanoparticle inks. Phys Status Solidi 209:2186–2194

[27] Soldano C, Mahmood A, Dujardin E (2010) Production, properties and potential of graphene. Carbon 48:2127–2150